

The halo mass dependence of physical and observable properties in the circumgalactic medium

Andrew W. S. Cook¹*, Freeke van de Voort¹, Rüdiger Pakmor² and Robert J. J. Grand³

¹Cardiff Hub for Astrophysics Research and Technology, School of Physics and Astronomy, Cardiff University, Queens Building, The Parade, Cardiff, CF24 3AA, UK

²Max-Planck-Institut für Astrophysik, Karl-Schwarzschild-Str. 1, D-85748, Garching, Germany

³Astrophysics Research Institute, Liverpool John Moores University, 146 Brownlow Hill, Liverpool, L3 5RF, UK

Accepted XXX. Received YYY; in original form ZZZ

ABSTRACT

We study the dependence of the physical and observable properties of the circumgalactic medium on its halo mass. We analyse 22 simulations from the Auriga suite of high resolution cosmological magneto-hydrodynamical ‘zoom-in’ simulations. We focus on the current epoch ($z = 0$) and halo masses between $10^{10} M_{\odot} \leq M_{200c} \leq 10^{12} M_{\odot}$. The median temperature and metallicity increase with halo mass as expected. We find a larger scatter in temperature and smaller scatter in metallicity at higher halo masses. The scatter of temperature and metallicity as a function of radius increases at larger radii. The median and scatter of the volume-weighted density and the mass-weighted radial velocity shows no significant dependence on halo mass. Our results highlight that the CGM is more multiphase in haloes at higher halo masses. We additionally investigate column densities for H I and the metal ions C IV, O VI, Mg II and Si II as a function of stellar mass and galactocentric radius. We find that the H I and metal ion column densities increase with the stellar mass of the system at sufficiently large radii ($R \gtrsim 0.2R_{200c}$). We find good agreement between our H I column densities and observations outside 20% of the virial radius and overpredict H I within 20%. Mg II and Si II are similarly overpredicted within 20% of the virial radius, but drop off steeply at larger radii. Our O VI column densities underpredict observations for stellar masses between $10^{9.7} M_{\odot} \leq M_{\star} < 10^{10.8} M_{\odot}$ with good agreement at $10^{10.8} M_{\odot}$. C IV column densities agree with observational detections above a halo mass of $10^{9.7} M_{\odot}$. We find that O VI (Mg II) traces the highest (lowest) temperatures, and lowest (highest) density and metallicity. OVI and CIV are photo-ionized (collisionally ionized) at low (high) halo masses with a transition to higher temperatures at $10^{11} M_{\odot}$. However, there is no clear trend for the radial velocity of the ions. These results demonstrate similarities and discrepancies between our simulations of Milky Way mass haloes and observations, as well as highlighting that further constraints are needed in less massive haloes.

Key words: galaxies: evolution – galaxies: haloes – galaxies: dwarf – MHD – cosmology: theory – methods: numerical

1 INTRODUCTION

The circumgalactic medium (CGM) is the gaseous component of dark matter-dominated haloes. It surrounds galaxies and contains gas accreted from the intergalactic medium (IGM) and gas ejected from the interstellar medium (ISM). The CGM plays a major role in the evolution of galaxies, acting as a reservoir for baryonic matter that can accrete on to the ISM and provide fuel for star formation (Tumlinson et al. 2017).

The CGM features various temperature phases which range from 10^4 K (or lower if we account for molecular outflows) up to approximately the virial temperature (or potentially hotter in outflows), with different phases in approximate pressure equilibrium. These gas phases are probed observationally primarily through absorption line spectroscopy as it is sensitive to the low densities in the CGM, making it an effective method of characterising the low-density CGM. Absorption line spectroscopy traces ions with different ionization potentials to detect various gas temperatures, and thus the multiphase

nature, of the CGM (Lehner et al. 2013; Anand et al. 2021; Mathur et al. 2021).

Quantifying the physical nature of the CGM is important to further our understanding of its role in galaxy evolution. We know from simulations and analytical arguments that the hydrodynamical properties of the CGM depend not only on feedback from the galaxy, but also on the halo mass (e.g. Frenk et al. 1988; Wang & Abel 2008; van de Voort & Schaye. 2012). Haloes with masses similar to the Milky Way ($10^{12} M_{\odot}$) are typically hot ($T \approx 10^6$ K) and metal-rich with higher accretion rates on to the galaxy than lower mass haloes (Kereš et al. 2005; Tumlinson et al. 2011).

Feedback from galaxies, driven by stellar winds, supernovae and active galactic nuclei (AGN), eject matter into the CGM which enriches the environment with metals (Muratov et al. 2015; Johnson et al. 2017; Sanchez et al. 2019). The strong feedback from star-forming galaxies means that only 20 – 25% of all metals produced are retained in their ISM (Peeples et al. 2014). Material ejected by these feedback processes either flows out of the CGM into the IGM and beyond, remains in the CGM, or re-accretes on to the galaxy. This re-accretion is likely important at late times as it can dominate the accretion rate (Oppenheimer et al. 2010; Hafen et al. 2020; Wright

* E-mail: cookaw@cardiff.ac.uk

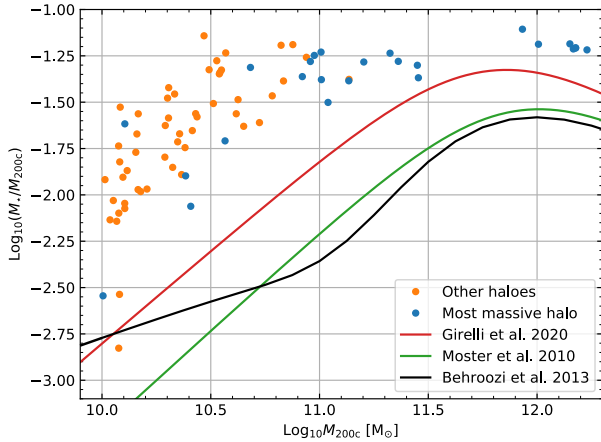


Figure 1. Stellar mass to halo mass (SM-HM) ratio against halo mass. Blue data points show the SM-HM ratio for the most massive halo from each simulation. We compare them to three models from [Moster et al. 2010](#), [Behroozi et al. 2013](#), and [Girelli et al. 2020](#) shown as green, black, and red curves respectively. Compared to these models, our simulations over-predict the SM-HM ratio but generally follow the same trend.

[et al. 2021](#)) and could be important for maintaining star formation in the galaxy.

Outflows from feedback also change the ionization states of metals by heating the gas. Low ionization states such as H I, Si II and Mg II trace cool gas ($T = 10^4$ K) in the CGM, with C IV tracing warmer gas of $10^{4.5-5}$ K, and higher ionization states such as O VI tracing warm-hot temperatures, if in collisional ionization equilibrium, of $10^{5.5}$ K ([Gnat & Sternberg 2007](#); [Wiersma et al. 2009](#); [Strawn et al. 2023](#)).

The ionization states of gas in the CGM can be probed in simulations too, utilising radiative transfer or non-equilibrium chemistry models (e.g. AREPO-RT and RAMSES-RTZ: [Kannan et al. 2019](#); [Katz 2022](#)) or post-processing tools such as TRIDENT ([Hummels et al. 2017](#)) which uses CLOUDY ([Ferland et al. 2017](#)) for its ionization tables. Mock observables have been compared to observations before with varying results. [Machado et al. \(2018\)](#) show over predictions in the O VI and Si III column densities when compared to observations. Studies also show good agreement for synthetic absorption lines and equivalent widths, and covering fractions from SIMBA consistent with observations ([Appleby et al. 2021](#)). The aim of these comparisons is to assist in constraining our models, thus leading to better predictions in future simulation work.

Observationally, little is known about the physical nature of the CGM around dwarf galaxies. While certain observations have been successful in measuring column densities and some properties of the CGM around dwarf galaxies (e.g. [Bordoloi et al. 2014](#); [Burchett et al. 2016](#); [Johnson et al. 2017](#); [Zheng et al. 2020](#); [Tchernyshyov et al. 2022](#); [Zheng et al. 2024](#)) the underlying physical nature is difficult to constrain. It is therefore important that we constrain the physical nature of the CGM of dwarf galaxies using cosmological simulations ([Peeples et al. 2019](#)).

In this work, we analyse cosmological zoom-in simulations to determine the dependence of the temperature, density, metallicity, and radial velocity on halo mass for haloes with a mass range of $10^{10} M_{\odot} \leq M_{200c} \leq 10^{12} M_{\odot}$. The aim of this work is to better understand the CGM in a cosmological context by quantifying the scatter in the temperature, density, metallicity and radial velocity

as a function of halo mass and galactocentric radius. Furthermore, we compare the column densities for H I, C IV, O VI, Mg II and Si II in our simulations with observational surveys including COS-Halos ([Tumlinson et al. 2013](#); [Werk et al. 2016](#)), COS-Dwarfs ([Bordoloi et al. 2014](#)) as well as other observational studies ([Johnson et al. 2015](#); [Zheng et al. 2024](#)) to better understand how our model compares to the existing observations and find discrepancies that we can use to inform future models.

This paper is structured as follows. We briefly outline the Auriga simulations, including how these haloes are selected in Sec. 2. We will then discuss the physical properties of the CGM in our simulated haloes in Sec. 3. We compare the results of our column densities to those from observations in Sec. 4. Finally, we conclude and discuss our results in Sec. 5.

2 THE AURIGA SUITE OF COSMOLOGICAL SIMULATIONS

This work studies the CGM of 22 high-resolution simulations from the Auriga project – a suite of magneto-hydrodynamical (MHD) cosmological zoom-in simulations ([Grand et al. 2017, 2024](#)). The simulations we use have a baryonic mass resolution of $\sim 6 \times 10^3 M_{\odot}$ (also referred to as ‘level 3’) and a dark matter resolution of $\sim 4 \times 10^4 M_{\odot}$.

We focus on gas within the virial radius (R_{200c}) of the halo, defined as the radius within which the density within it is approximately 200 times the critical density of the universe. We study haloes within a halo mass range of $10^{10} M_{\odot} \leq M_{200c} \leq 10^{12} M_{\odot}$, corresponding to a stellar mass range of $10^{7.5} M_{\odot} \leq M_{\star} \leq 10^{11} M_{\odot}$. For six simulations, the most massive halo at the centre of the zoom region has a halo mass between $10^{10} M_{\odot} - 10^{11} M_{\odot}$, 12 between $10^{11} M_{\odot} - 10^{11.5} M_{\odot}$ and six between $1 \times 10^{12} M_{\odot} - 2 \times 10^{12} M_{\odot}$. Table A1 in the Appendix lists further information on the key properties of the most massive haloes in each of the 22 zoom-in simulations. The following is a brief overview of the simulations and a description of the post-processing method to obtain metal ion column densities.

Figure 1 shows the ratio of stellar mass to halo mass as a function of halo mass. This includes the 22 most massive haloes and 64 additional haloes within the zoom-in region of each simulation. We find our simulations overestimate the stellar mass based on abundance matching from [Moster et al. \(2010\)](#), [Girelli et al. \(2020\)](#) and [Behroozi et al. \(2013\)](#). The larger scatter of lower mass haloes has also been found in other simulation suites with an explicit ISM model ([Agertz et al. 2020](#); [Gutcke et al. 2021](#); [Sales et al. 2022](#)).

The initial conditions of Auriga are based on the dark matter-only simulations from the EAGLE project ([Schaye et al. 2015](#)), with a co-moving box size of 100 Mpc. Haloes are identified using a friends-of-friends (FoF) algorithm with a standard linking length ([Davis et al. 1985](#)). Haloes are selected based on their halo mass then by how isolated those haloes are, of which the halo selected for zoom is randomly selected from the lowest percentile. The mass selection criterion for Milky Way mass haloes is $0.5 < M_{200c}/10^{12} M_{\odot} < 2$ and less massive haloes were selected within $0.5 < M_{200c}/10^{11} M_{\odot} < 5$ and $0.5 < M_{200c}/10^{10} M_{\odot} < 5$. The high resolution zoom-in region extends to $\approx 5R_{200c}$ of each halo. Auriga adopts cosmological parameters $\Omega_m = 0.307$, $\Omega_b = 0.048$ and $\Omega_{\Lambda} = 0.693$ with $H_0 = 100h \text{ km s}^{-1} \text{ Mpc}^{-1}$ where $h = 0.6777$ from [Planck Collaboration et al. \(2014\)](#).

The simulations were run from $z = 127$ to $z = 0$ using the arbitrary Lagrangian-Eulerian moving-mesh code AREPO ([Springel 2010](#)), which includes magneto-hydrodynamics (MHD) for gas and

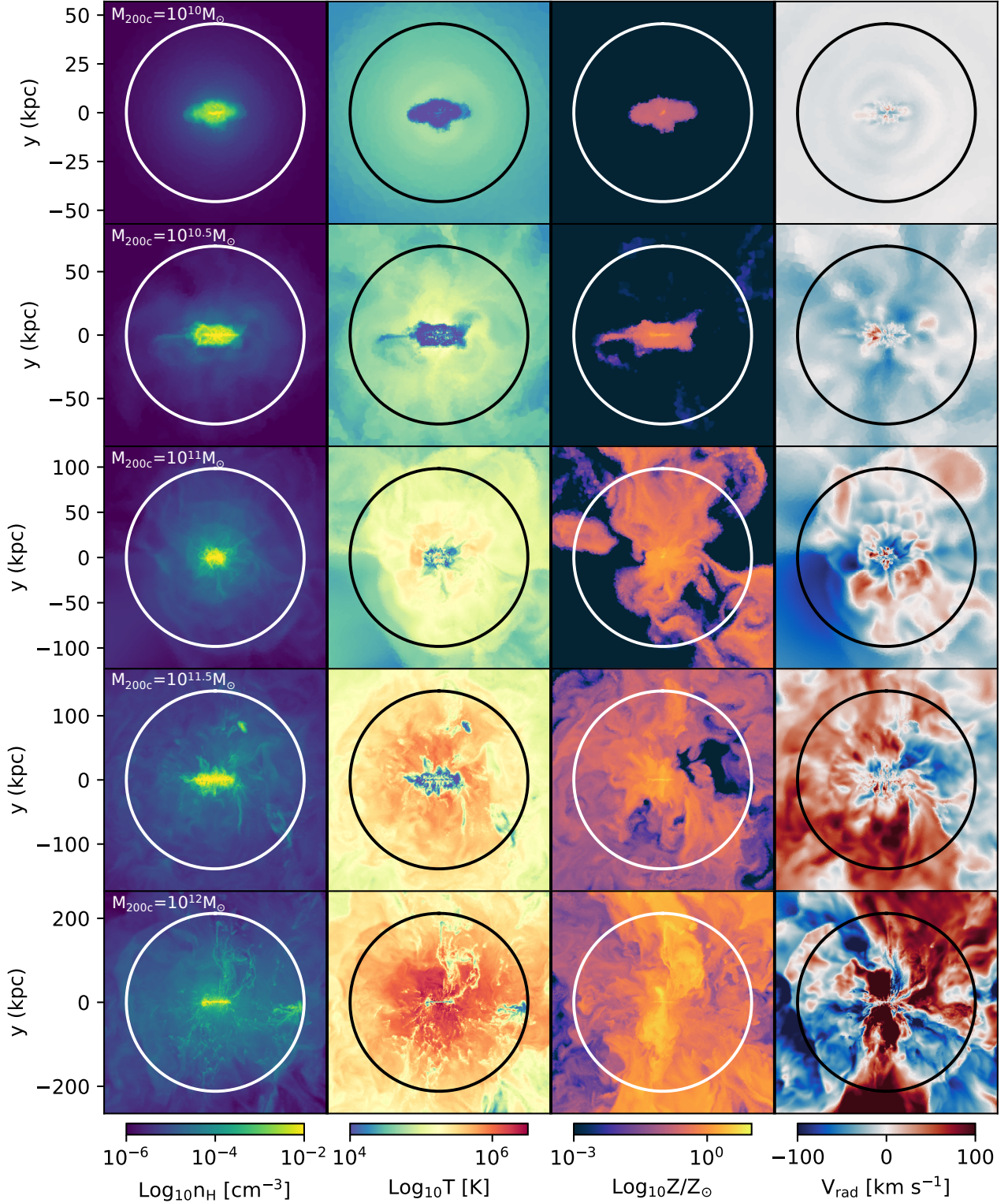


Figure 2. $2.5R_{200c} \times 2.5R_{200c}$ thin projections of five haloes, rotated such that the stellar disc is edge-on. Columns show, from left to right, the volume-weighted hydrogen number density and mass-weighted temperature, metallicity, and radial velocity with a projection depth of $R_{200c}/8$. The halo mass increases from top to bottom from $10^{10} M_{\odot}$ – $10^{12} M_{\odot}$ in steps of 0.5 dex. The circle in each panel indicates the virial radius of each halo. When compared to high-mass haloes, low-mass haloes ($M_{200c} < 10^{11} M_{\odot}$) show smaller scatter in the temperature, the density, the metallicity and the radial velocity. The metallicity of the low-mass haloes is highest in the centre but is still several orders of magnitude lower than the solar values of high-mass haloes with a sharp and steep drop off in metallicity outside of the centre. The radial velocities are also significantly lower.

collisionless dynamics (for dark matter, stars and black holes). AREPO uses an unstructured Voronoi mesh with idealised MHD solved by a finite volume second order Runge-Kutta integration scheme (Pakmor et al. 2016).

The Auriga galaxy formation model is described fully in Grand et al. (2017) and summarised here. The ISM subgrid model in these simulations is described in Springel & Hernquist (2003) as a two-phase medium of dense, cold gas clouds surrounded by hotter, ambient gas. The gas in the ISM is assumed to be star-forming once the density exceeds a threshold density of $n_{\text{H}}^* = 0.13 \text{ cm}^{-3}$. These simulations additionally include primordial and metal line-cooling (Vogelsberger et al. 2013) as well as an ultraviolet background with self-shielding (Faucher-Giguère et al. 2009; Rahmati et al. 2013).

Auriga incorporates feedback from supernovae, stellar winds and AGN. Stellar feedback is implemented through gas cells that are temporarily converted into collisionless wind particles, ejected from star-forming gas, until they reach 5% of n_{H}^* where they recouple and deposit mass, momentum, thermal energy and metals. The minimum temperature in our simulations is set to 10^4 K because cooling below this temperature is inefficient.

AGN feedback is modelled as a two-mode process: one which heats the gas locally around the black hole and the other which gently heats bubbles of gas at randomly placed locations up to 80% of the virial radius. Black holes are seeded in the simulations with a mass of $10^5 h^{-1} M_{\odot}$ when the FoF halo group has a mass $M_{\text{FOF}} = 5 \times 10^{10} h^{-1} M_{\odot}$. Ionising radiation is also included in the AGN feedback model in the form of X-rays.

We calculate the column density of H I, C IV, O VI, Mg II and Si II in our simulations. We chose these ions because they are the most commonly observed ions through absorption line spectroscopy (Fox et al. 2005; Ranjan et al. 2022) and trace different temperature phases of the gas. The mass fraction of H I is calculated on-the-fly whereas the mass fraction of the metal ions are calculated in post-processing. We use tables generated with CLOUDY (Ferland et al. 2017) by Hummels et al. (2017) to compute the mass fraction of the ions. We can then use this ion fraction and the metal specific mass fraction to calculate the column density along any sight-line in our simulations.

A resolution test was conducted comparing this set of 22 simulations with different mass resolutions: $\sim 8 \times 10^2 M_{\odot}$ (also referred to as 'level 2') and $\sim 5.4 \times 10^4 M_{\odot}$ (also referred to as 'level 4'). The level 2 simulations all had halo masses $\leq 10^{10.5} M_{\odot}$ and the level 4 simulations had halo masses $\geq 10^{11} M_{\odot}$.

3 DEPENDENCE OF PHYSICAL PROPERTIES IN THE CGM ON HALO MASS

One of the most difficult components of the CGM to observationally constrain is the physical properties including its temperature, density, metallicity and radial velocity. While the temperature can be inferred, the CGM properties are largely unconstrained, especially in low-mass haloes. We use our cosmological simulations to quantify the temperature, density, metallicity and radial velocity as a function of halo mass and radius to obtain a broad understanding of the physical nature of the CGM in our simulations.

3.1 Physical Nature of the CGM

Figure 2 shows thin projections at $z = 0$ of the volume-weighted density and mass-weighted temperature, metallicity, and radial velocity for five haloes rotated such that the central galaxy is edge-on.

The halo mass ranges from $10^{10} M_{\odot}$ – $10^{12} M_{\odot}$, increasing in mass intervals of 0.5 dex from top to bottom. The circles indicate the virial radius of each halo: 45 kpc, 70 kpc, 98 kpc, 139 kpc, and 212 kpc, from top to bottom.

For more massive haloes, the CGM is hotter, more enriched with metals, and has higher radial velocities, both inflowing (negative values) and outflowing (positive values). In our most massive halo (bottom row) bipolar outflows can be seen along the minor axis which have high metallicity and radial velocities but show no significant temperature differences along this axis. High values along the minor axis are seen in radial velocity and metallicity but are lower along the major axis. The temperature and density typically decrease with radius with minor differences outside of the central $0.25R_{200c}$.

In contrast, our lowest mass haloes (top row) exhibit low scatter in their temperature, density, metallicity and radial velocity. High values of each property are found in the centre of the halo. Because the radial velocity is low and the gas is mostly inflowing, metals cannot reach significant distances into the CGM, resulting in a deficit in metals in the outer CGM. Similarly the temperature of the CGM does not change significantly outside of the central $0.25R_{200c}$. Temperatures reach $\sim 10^{4.5} \text{ K}$ at most and do not fluctuate much at fixed radii.

Figure 3 shows the density, temperature, metallicity and radial velocity as a function of halo mass for 86 haloes within the zoom-in region of our 22 simulations. We calculate the median and 16th and 84th percentile scatter for the gas within $0.3R_{200c}$ – $1.0R_{200c}$ to exclude the dense, cool gas in the centre. The blue circles show mass-weighted values and the orange squares show volume-weighted values. For clarity, the scatter is only shown for mass-weighted temperature, metallicity and radial velocity and for the volume-weighted density. We additionally include the virial temperature from Mo et al. (2010) in the temperature panel.

As expected, we find that the median temperature is higher in more massive haloes, increasing from $\sim 10^{4.0} \text{ K}$ in our lowest mass haloes ($M_{200c} = 10^{10} M_{\odot}$) up to temperatures of $\sim 10^6 \text{ K}$ at high masses ($M_{200c} = 10^{12} M_{\odot}$). Furthermore, the scatter is wider at these high masses, with a range of ~ 0.5 dex in low-mass haloes, increasing to ~ 1.5 dex in high-mass haloes. This increase indicates that the CGM is more multiphase in more massive haloes. The 16th percentile of most of our haloes above $M_{200c} > 10^{11.75} M_{\odot}$ haloes are at temperatures above 10^4 K . Cool gas is still present just not in large quantities.

The gas density shows no clear dependence on the halo mass. The scatter fluctuates by < 0.1 dex from halo to halo, but shows no clear trend with halo mass for either mass- or volume-weighted quantities. The scatter seen here is primarily caused by the decreasing trend in the average density from $0.3R_{200c}$ to R_{200c} (see Figure 4).

The median metallicity has no clear dependence on halo mass for $M_{200c} < 10^{11} M_{\odot}$ (low-mass haloes), with more metal-rich gas present in more massive haloes; median values cover a range from $\sim 10^{-5}$ – 10^{-1} in low-mass haloes to near solar values ($\sim 10^0$) in more massive haloes ($M_{200c} \geq 10^{11} M_{\odot}$). The scatter is small in more massive haloes, decreasing from ~ 4 ($\leq 10^{-5}$ – $10^{-0.5}$) dex to ~ 1 dex (10^{-1} – 10^0) over our sample of haloes. We find that the most massive haloes in the zoom-in region, which were selected to be the most isolated, exhibit low metallicities. It is therefore possible that additional haloes located within the zoom-in region have gained metals from nearby systems. The stronger feedback from more massive galaxies produces stronger outflows, therefore contributing to more metal enrichment in the outer CGM of more massive haloes.

The median radial velocity is about -40 – 40 km/s across the halo mass range. Inflows dominate slightly over outflows, but shows no clear dependence on halo mass. The scatter in radial velocity is more

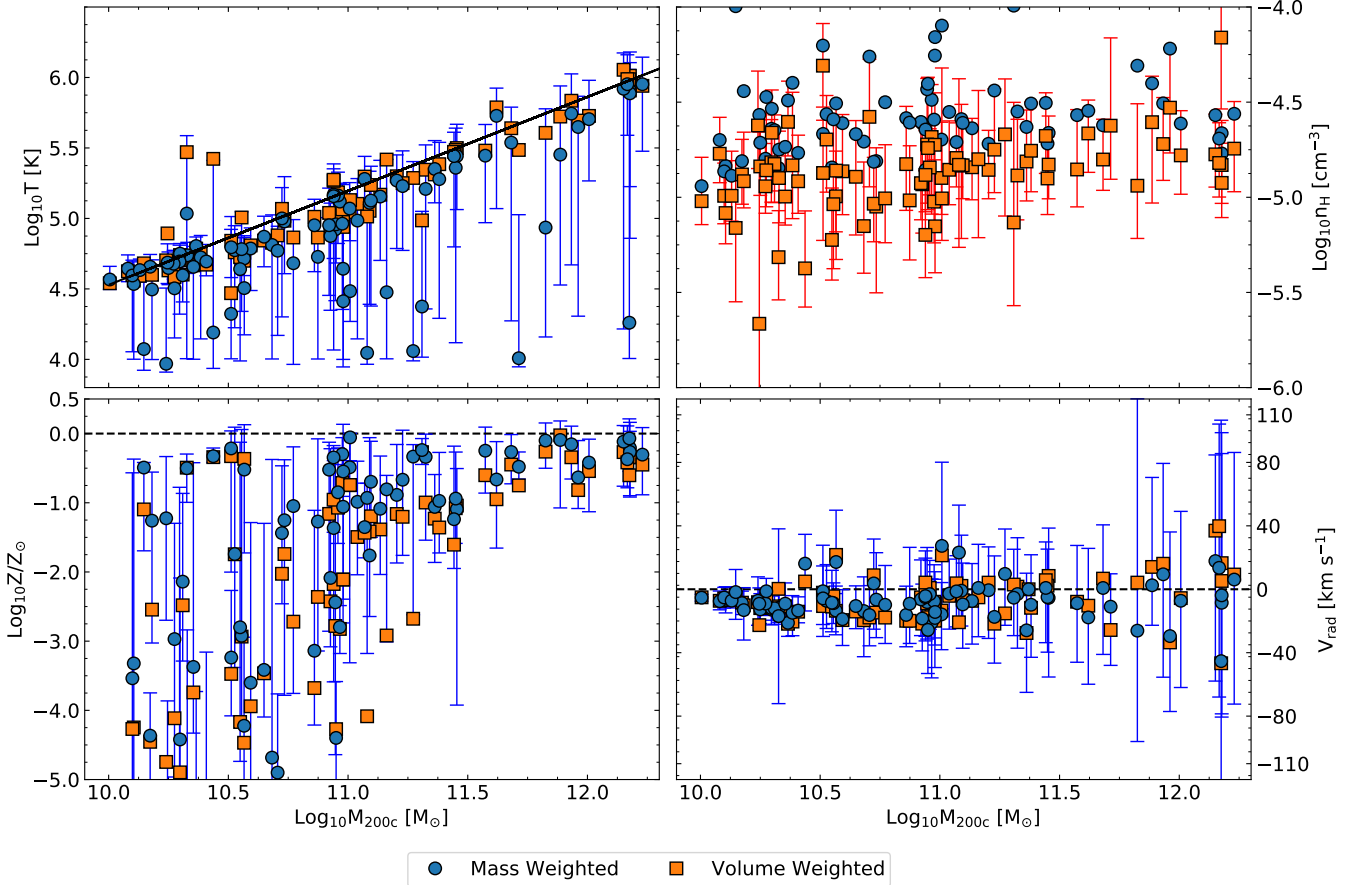


Figure 3. Median CGM temperature (top, left), hydrogen number density (top, right), metallicity (bottom, left) and radial velocity (bottom, right) for 86 haloes within the zoom-in region of our simulations as a function of halo mass with scatter bars showing the 16th and 84th percentiles. The median shown is volume-weighted (orange squares) for density and mass-weighted (blue circles) for the other properties. The scatter is only shown for mass-weighted temperature, metallicity and radial velocity and for the volume-weighted density. We additionally include the virial temperature from Mo et al. (2010) in the temperature panel. The properties are measured between $0.3 \leq R/R_{200c} \leq 1.0$ to remove the central galaxy and its extended H I-dominated disc. The temperature and metallicity vary strongly for our haloes, both in their median values and their scatter. There is no clear dependence on halo mass for the density. The scatter in radial velocity is wider in more massive haloes. However, the median radial velocity shows no clear trend with halo mass and is in most cases dominated by inflows.

skewed towards inflows in less massive haloes ($M_{200c} < 10^{11.5} M_{\odot}$) while more massive haloes show more balanced inflows and outflows.

The relationship between volume- and mass-weighted quantities changes for different properties. The volume- and mass-weighted values of temperature and radial velocity are similar. The volume-weighted metallicity is typically lower than the mass-weighted metallicity in low-mass haloes ($M_{200c} < 10^{11} M_{\odot}$) though the difference is smaller in more massive haloes indicating metals are clumped in higher density gas.

3.2 Radial Profiles

Figure 4 shows the radial dependence of the temperature, density, metallicity and radial velocity, for both inflowing (solid line) and outflowing (dashed line) gas, for the same five haloes as shown in Figure 2. The solid curves show the median properties and the shaded region the 16th and 84th percentile scatter. The haloes shown range in halo mass from $10^{10} M_{\odot}$ – $10^{12} M_{\odot}$, increasing from left to right in steps of 0.5 dex. Properties are mass-weighted except density which is volume-weighted. We exclude star-forming gas from this figure.

The median temperature remains fairly constant at 10^4 K in the inner CGM (typically between $0.1 - 0.25 R_{200c}$ with some variation

between haloes). This region is dominated by a non-star-forming extended gas disc. As matter accretes onto the CGM, the temperature has been shown to increase to values near the virial temperature (van de Voort & Schaye, 2012). When the gas reaches higher densities in the inner CGM, it is able to cool and join the central disc. The scatter in temperature of the gas in the outer CGM is larger in more massive haloes, indicating that the gas in the outer CGM ($R > 0.25 R_{200c}$) is more multiphase compared to less massive haloes.

The highest densities (10^{-1}cm^{-3}) are found in the centre of the CGM, typically within $0.25 R_{200c}$, decreasing down to 10^{-5}cm^{-3} at the virial radius. The scatter is most notable in our $10^{10} M_{\odot}$ haloes with very low scatter outside of $0.25 R_{200c}$. The scatter above this halo mass is generally consistent for all other haloes. We see a radial dependence in the median profile but no change in scatter or halo mass dependence on gas density when volume-weighted. We separately calculated the mass-weighted density which showed the same median trend as volume-weighted density. The density remains high at $\sim 10^{-1} \text{cm}^{-2}$ out to larger radii than volume-weighted, typically out to $0.25 R_{200c}$, before a sharp drop in density. Additionally, mass-weighted density shows somewhat higher scatter in more massive haloes.

The highest metallicity is seen in the centre of our haloes in the

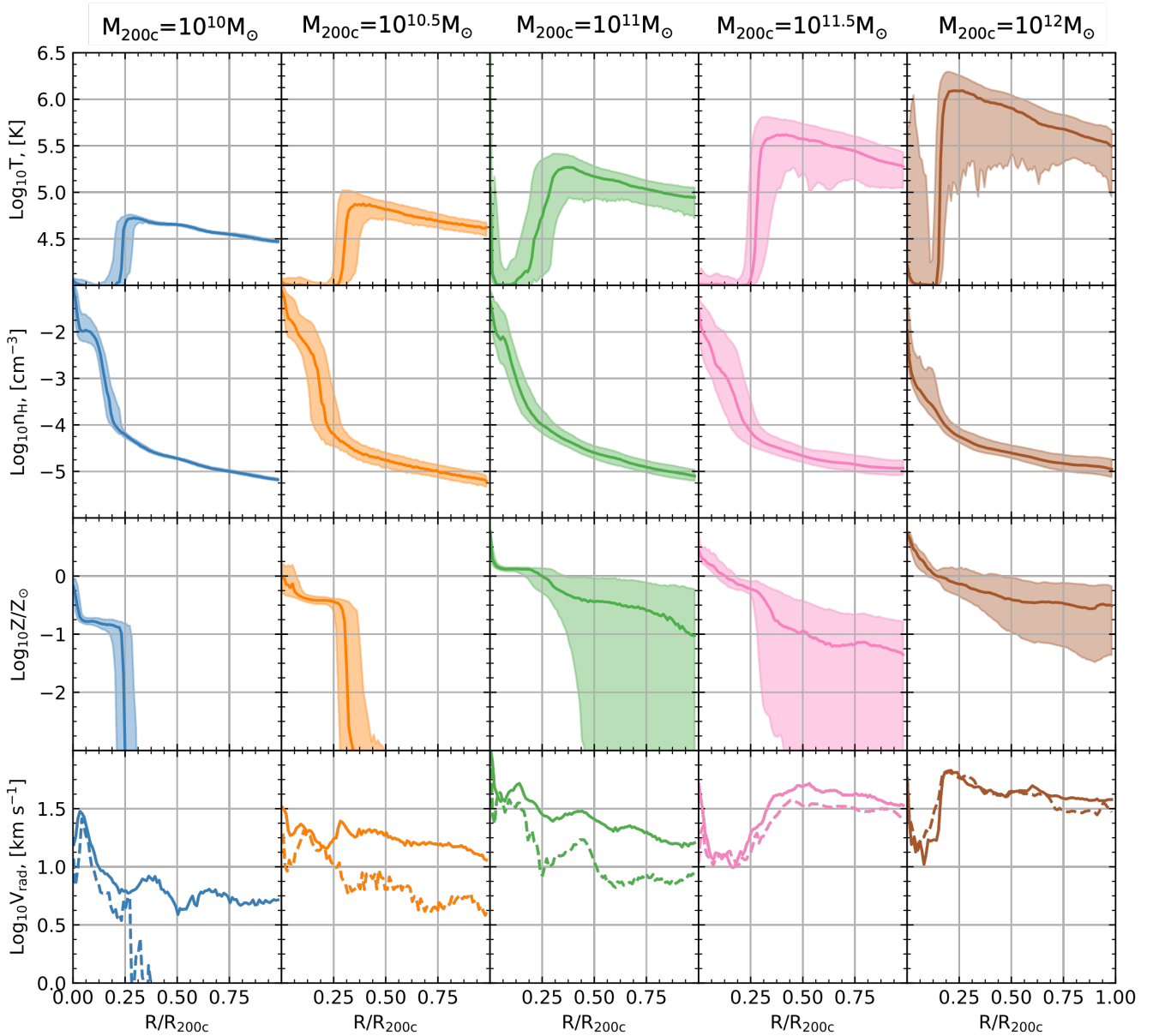


Figure 4. Median physical properties from top to bottom: temperature, density, metallicity and radial velocity as a function of radius normalised by the virial radius. Shaded regions show the 16th and 84th percentile of the properties as a measure of the scatter for the haloes from Fig. 2. The halo mass increases from left to right, from $10^{10} M_{\odot}$ – $10^{12} M_{\odot}$ in steps of 0.5 dex. The temperature, metallicity and radial velocity are mass-weighted whereas the density is volume-weighted. Gas associated with satellites and the ISM has been excluded. The temperature profile decreases at $R > 0.3R_{200c}$ with a steeper decrease in more massive haloes. The metallicity is highest in the centre in all haloes. Haloes with $M_{200c} \leq 10^{10.5} M_{\odot}$ have a steep drop off at radii larger than $0.25R_{200c}$. For $M_{200c} > 10^{10.5} M_{\odot}$, the metallicity profile is much shallower and the scatter is large. Reasonably metal-rich gas can be found in the outer CGM as well as metal-poor gas. Similar to Figure 3, the density shows no strong dependence on halo mass, with a steep drop off in the inner $0.25R_{200c}$ CGM and a more shallow profile in the outer CGM. Finally, the outflows in $M_{200c} \leq 10^{11} M_{\odot}$ haloes is significantly weaker than the inflowing matter. In more massive haloes, the inflows and outflows are at approximately equal rates.

inner $\sim 0.25R_{200c}$. For our low-mass dwarfs, $M_{200c} < 10^{11} M_{\odot}$, the metallicity decreases sharply because the outflows do not reach larger distances. The central metallicity is 1 dex lower in the $10^{10} M_{\odot}$ halo compared to the $10^{11} M_{\odot}$ halo. For more massive haloes ($M_{200c} \geq 10^{11} M_{\odot}$) the median metallicity following a decreasing profile, with the scatter increasing with radius.

We see higher inflow and outflow velocities for more massive haloes. Both inflows and outflows follow similar trends within $0.25R_{200c}$ for all haloes. Haloes with $M_{200c} < 10^{11.5} M_{\odot}$ have lower

radial velocities in outflowing gas compared to inflowing gas outside of $0.25R_{200c}$, and are thus dominated by inflowing gas out to the virial radius. More massive haloes feature faster inflows than low mass haloes and similarly high outflows. Haloes with $M_{200c} \geq 10^{11.5} M_{\odot}$ exhibit inflowing and outflowing gas increasing to a maximum radial velocity at roughly the same radius as the maximum temperature. At this point, the gas is in rotation leading to less inflowing and outflowing velocities.

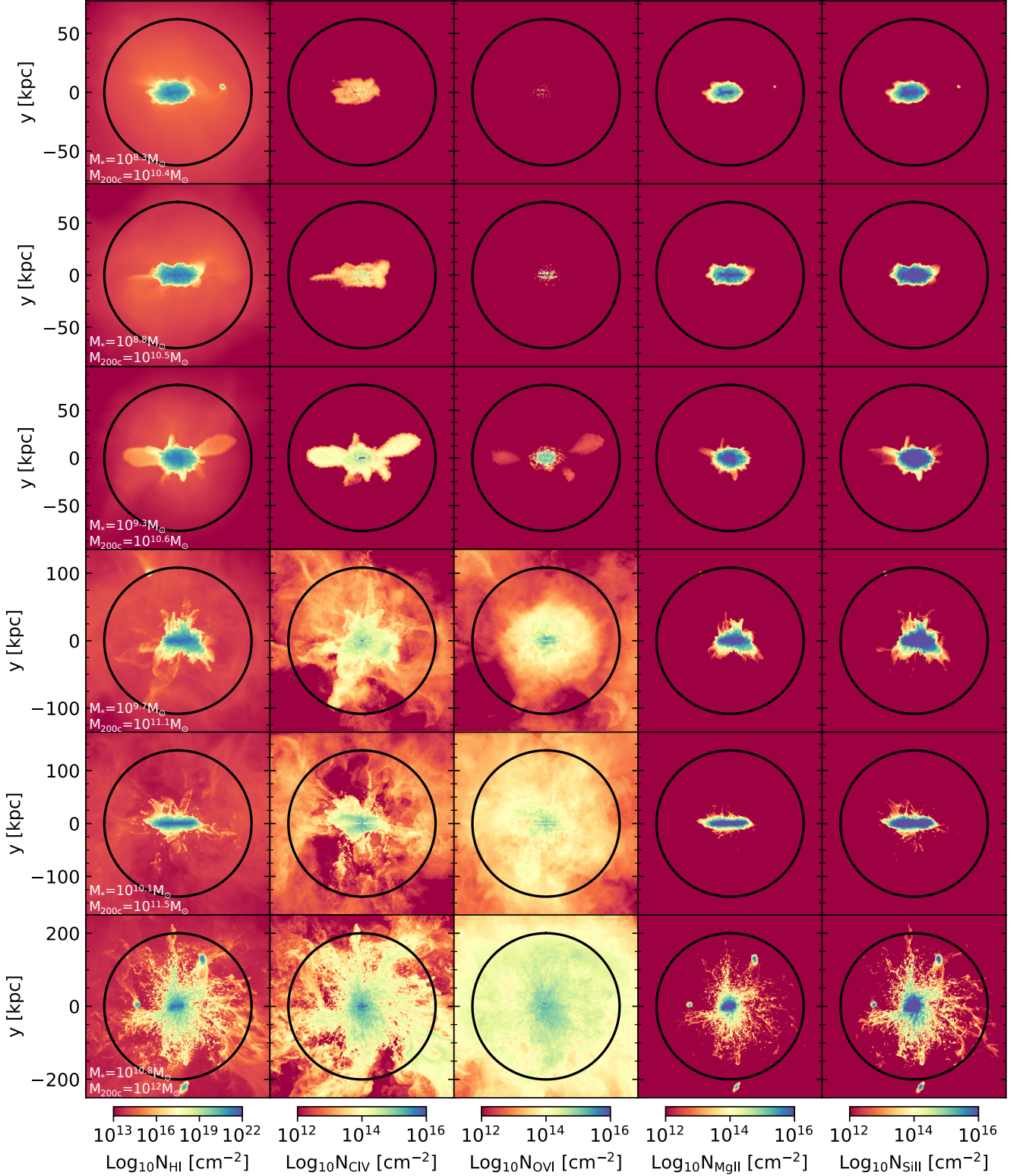


Figure 5. $2.5R_{200c} \times 2.5R_{200c}$ projections of six haloes with a depth of $2R_{200c}$, rotated such that the stellar disc is edge-on. The chosen haloes are selected based on the stellar mass of the central galaxies and are thus different from those in Figure 2. From top to bottom the stellar masses increase from $10^{8.3} M_{\odot}$, $0^{8.8} M_{\odot}$, $10^{9.3} M_{\odot}$, $10^{9.7} M_{\odot}$, $10^{10.1} M_{\odot}$ to $10^{10.8} M_{\odot}$. From left to right, columns correspond to H I , C IV , O VI , Mg II and Si II . The virial radius is indicated by the black circle in each panel. Column densities are highest in the centres of all haloes and decrease with radius. $N_{\text{C IV}}$ and $N_{\text{O VI}}$ increase with stellar mass, reaching high values even in the outer CGM.

4 COLUMN DENSITY OF THE CGM

It is important to understand how our simulations match or differ from observations. This will assist in understanding the validity of our models and how best we can improve them in future simulations.

We compare the column density (N_x where x is H I, C IV, O VI, Si II or Mg II) of H I, C IV, O VI, Si II and Mg II in our simulations with observational data from [Bordoloi et al. \(2014\)](#), [Werk et al. \(2013\)](#), [Tumlinson et al. \(2013\)](#), [Johnson et al. \(2015\)](#), and [Zheng et al. \(2024\)](#). We exclude observational errors as they are $\approx \pm 0.01 - 0.15$ and are therefore negligible compared to the scale of the scatter of our simulations. The CGM is ionized via photo-ionization and collisional ionization. The level of ionization depends on the density and temperature of the gas, as well as the redshift (e.g. [Strawn et al. 2023](#)). We define two temperature regimes: the warm regime which is traced by C IV and O VI at temperatures of $T = 10^{4.5} \text{ K} - 10^{5.5} \text{ K}$, and a cool regime, traced by H I, Mg II and Si II at temperatures of $T = 10^{4.0} \text{ K} - 10^{4.5} \text{ K}$.

Figure 5 shows halo projections oriented edge-on to the galactic stellar disc of, from left to right, $N_{\text{H I}}$, $N_{\text{C IV}}$, $N_{\text{O VI}}$, $N_{\text{Mg II}}$ and $N_{\text{Si II}}$. Six different haloes are chosen based on their stellar mass. The six haloes have stellar masses between $10^{8.3} M_{\odot} - 10^{10.8} M_{\odot}$ increasing from top to bottom in steps of 0.5 dex. High column densities of H I and our metal ions are seen in the centres of these haloes. The low ionization state ions highlight the filamentary structure of the outer CGM in the most massive haloes ($M_{\star} = 10^{10.8} M_{\odot}$). We find low $N_{\text{C IV}}$ and $N_{\text{O VI}}$ in the outer CGM of galaxies with $M_{\star} \leq 10^{9.5} M_{\odot}$ ($M_{200c} \leq 10^{11.0} M_{\odot}$). $N_{\text{C IV}}$ and $N_{\text{O VI}}$ are higher in the outer CGM of more massive haloes, because these haloes contain higher temperature gas.

4.1 Column Density and Stellar Mass

Figure 6 shows the various column densities as a function of stellar mass. The median is shown as red circles and the scatter is quantified with 16th and 84th percentiles and shown as scatter bars. The median and percentiles are calculated along two orthogonal axes for which the central galaxy has been rotated to be edge-on. We split these data into three radial bins of $0.0R_{200c} - 0.2R_{200c}$ (central CGM), $0.2R_{200c} - 0.4R_{200c}$ (inner CGM) and $0.4R_{200c} - 0.6R_{200c}$ (intermediate CGM). Observational detections are shown as filled squares, upper limits as open downward arrows, and lower limits as open upward arrows. We additionally set the ion fraction to zero in the ISM.

The median and scatter of $N_{\text{H I}}$ decreases with radius for all stellar masses. In the central CGM, our median $N_{\text{H I}}$ over-predicts observations though there is significant scatter towards lower column densities. The median $N_{\text{H I}}$ in the inner CGM decreases to $\sim 10^{14} \text{ cm}^{-2} - \sim 10^{15} \text{ cm}^{-2}$ where we find our simulations agree reasonably well with observations. In the intermediate CGM, most observational data at $M_{\star} > 10^9 M_{\odot}$ are somewhat higher than our median column densities for H I. However, our haloes also show significant scatter towards higher column densities. Observations also show substantial scatter throughout the CGM, with most $N_{\text{H I}}$ detections falling within the upper percentile of our scatter above a stellar mass of $10^9 M_{\odot}$.

The median $N_{\text{Mg II}}$ and $N_{\text{Si II}}$ follow a similar trend to H I for all stellar masses: an over-prediction compared to the observational data in the centre and a decrease with radius which leads to values more in agreement with observations. Column densities range from 10^{14} cm^{-2} to 10^{16} cm^{-2} in the centre and follow a decreasing radial trend. The median values of $N_{\text{Si II}}$ fall within the range of observed

values and upper limits for $M_{\star} > 10^{9.5} M_{\odot}$ in the inner CGM and underpredict observations in the intermediate CGM. The median $N_{\text{Mg II}}$ is typically ~ 1 dex lower than a systems Si II and underpredicts observations in both the inner and intermediate CGM. This is partially due to the underproduction of Mg following the yield set of ([Portinari et al. 1998](#)). For $M_{\star} \leq 10^{9.5} M_{\odot}$, $N_{\text{Mg II}}$ and $N_{\text{Si II}}$ decrease to values that would be undetectable in observations.

We find similar median $N_{\text{C IV}}$ values to those observed within the central CGM for all stellar masses. $N_{\text{C IV}}$ increases with stellar mass up to $10^{9.5} M_{\odot}$ beyond which the column density remains constant. The median $N_{\text{C IV}}$ decreases and its scatter increases with increasing radii. The most significant decrease in median $N_{\text{C IV}}$ is seen in haloes with $M_{\star} \leq 10^{9.5} M_{\odot}$. A larger increase in the scatter of $N_{\text{C IV}}$ occurs in haloes below a stellar mass of $10^{9.5} M_{\odot}$. From the central CGM to the inner CGM, our median $N_{\text{C IV}}$ decreases by ~ 2 dex from $10^{13} \text{ cm}^{-2} - 10^{14} \text{ cm}^{-2}$ to $10^{11} \text{ cm}^{-2} - 10^{13} \text{ cm}^{-2}$. This is below observational detections for $M_{\star} \leq 10^{9.5} M_{\odot}$. This decrease also happens in the intermediate CGM by about the same ~ 2 dex, leading to a total decrease of ~ 4 dex. For $M_{\star} > 10^{9.5} M_{\odot}$, $N_{\text{C IV}}$ decreases by ~ 2 dex from from the central to the intermediate CGM and largely agrees with observations.

Our $N_{\text{O VI}}$ agrees with observational detections for $M_{\star} > 10^{9.5} M_{\odot}$ in the central CGM. The median $N_{\text{O VI}}$ decreases by ~ 1 dex from the central CGM ($N_{\text{O VI}} = 10^{14} - 10^{15} \text{ cm}^{-2}$) to the inner CGM ($N_{\text{O VI}} = 10^{13} - 10^{14} \text{ cm}^{-2}$) at these stellar masses. At larger radii, the systems with $M_{\star} > 10^{10.7} M_{\odot}$ have a less significant decrease than systems below $10^{10.7} M_{\odot}$ and remain in agreement with observational detections. For $M_{\star} \leq 10^{9.5} M_{\odot}$, the median $N_{\text{O VI}}$ is $\sim 3 - 4$ dex lower than in more massive systems. The scatter in $N_{\text{O VI}}$ is small for $M_{\star} > 10^{9.5} M_{\odot}$ but larger at low masses. For all radial bins, $N_{\text{O VI}}$ is substantially higher above $10^{9.5} M_{\odot}$.

4.2 Radial Profiles of Column Density

Figure 7 shows the radial dependence of the median and 16th and 84th percentiles for, from top to bottom, $N_{\text{H I}}$, $N_{\text{C IV}}$, $N_{\text{O VI}}$, $N_{\text{Mg II}}$ and $N_{\text{Si II}}$ compared with observational data using impact parameter as a proxy for radius. We binned the observational data by stellar mass between $10^8 M_{\odot} - 10^{11} M_{\odot}$ in equal intervals of 0.5 dex from left to right. We show the same simulated haloes as in Figure 5 which have a stellar mass that is as close to the middle of the stellar mass bin as possible.

Our H I column density shows a steep decrease from $\sim 0.3R_{200c}$. At larger radii, the column density features a shallower decrease out to the virial radius for all haloes up to and including $10^{10.1} M_{\odot}$. The scatter of H I is similar for all haloes up to $10^{10.8} M_{\odot}$ in the inner $0.3R_{200c}$. At a stellar mass of $10^{10.8} M_{\odot}$, we see significantly wider scatter beyond $0.3R_{200c}$ and shallower decrease than at lower stellar masses out to $\sim 0.7R_{200c}$. The H I column density in observations is fairly constant between a stellar mass of $10^{8.3} M_{\odot} - 10^{9.3} M_{\odot}$, matching our simulated radial profiles at $\sim 10^{14} \text{ cm}^{-2}$. For $10^{9.7} M_{\odot} \leq M_{\star} \leq 10^{10.1} M_{\odot}$, our simulations underpredict $N_{\text{H I}}$ outside of $0.5R_{200c}$ and match at smaller radii. At $10^{10.8} M_{\odot}$, we see better agreement between $0.25R_{200c} - 0.75R_{200c}$ and observations but an overprediction at $R < 0.25R_{200c}$.

The column densities of C IV and O VI steeply decrease with radius for $M_{\star} \leq 10^{9.3} M_{\odot}$. $N_{\text{C IV}}$ and $N_{\text{O VI}}$ are higher in the outer CGM in haloes with $M_{200c} \geq 10^{11} M_{\odot}$ or $M_{\star} \geq 10^{9.7} M_{\odot}$. This is likely because of stronger outflows, and because the gas in these haloes has a higher virial temperatures than in smaller haloes. This means there

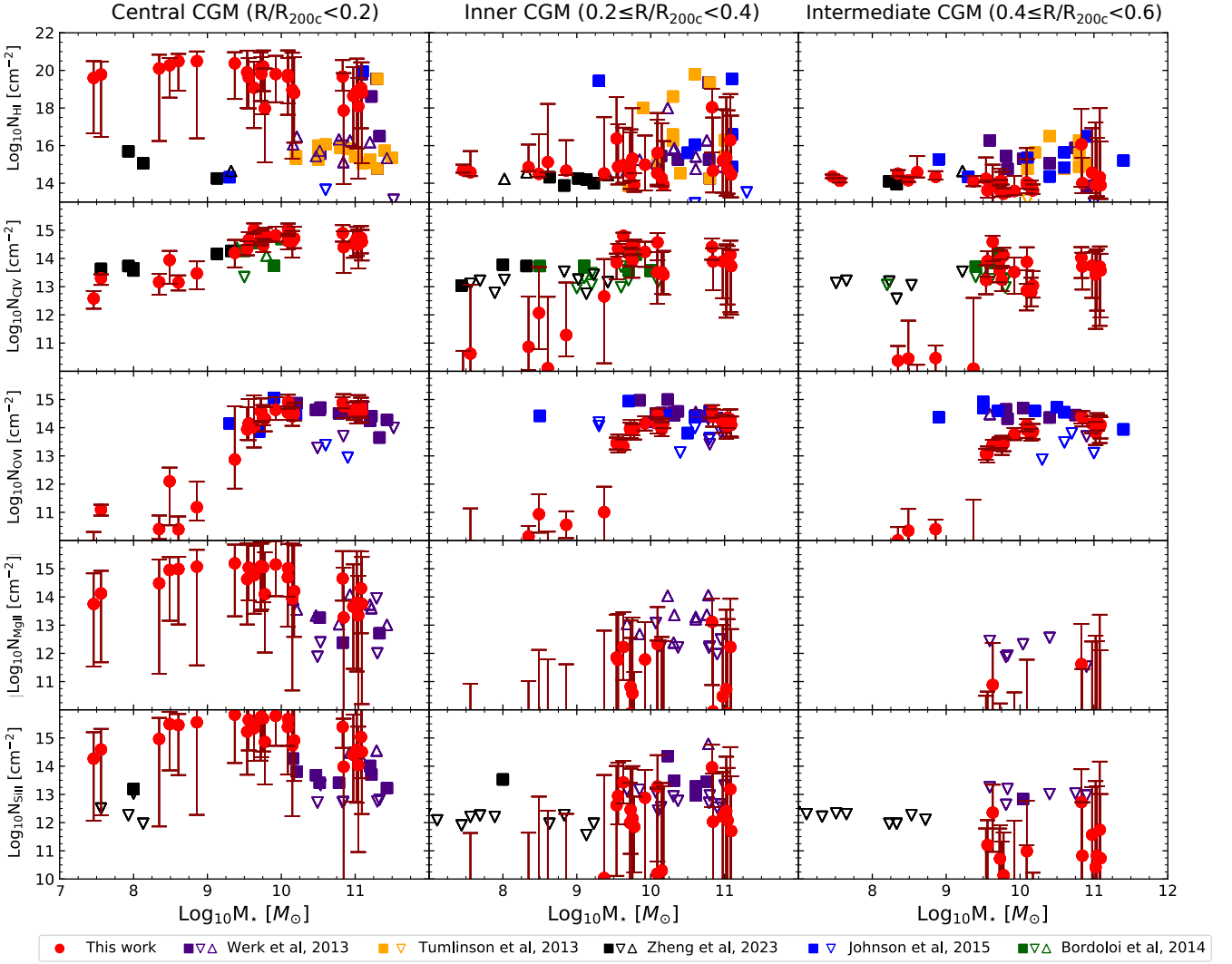


Figure 6. Simulated and observed column densities as a function of M_* . From top to bottom, red circles show the median of $N_{\text{H I}}$, $N_{\text{C IV}}$, $N_{\text{O VI}}$, $N_{\text{Mg II}}$ and $N_{\text{Si II}}$ with 16th and 84th percentile scatter bars. We separate the column densities within $0.6R_{200c}$ in three radial bins of $0.2R_{200c}$ width. The depth of the projection is $2R_{200c}$ and the median is measured along two orthogonal edge-on directions. We compare with observational data from [Werk et al. \(2013\)](#), [Tumlinson et al. \(2013\)](#), [Bordoloi et al. \(2014\)](#), [Johnson et al. \(2015\)](#) and [Zheng et al. \(2024\)](#). Detections are shown as filled squares and upper (lower) limits as empty downwards (upwards) arrows. The observational error bars are omitted for readability. Additionally, the ISM is removed from our measurements to select only CGM gas of the main halo. The column density of warm ions (C IV and O VI) is high above $10^{9.5} M_\odot$ stellar mass haloes for all radial bins. C IV is relatively constant above $M_* = 10^{9.5} M_\odot$ and agrees with detections at all radii for higher mass haloes and in lower mass haloes within $0.2R_{200c}$. Lower mass systems have significantly lower column densities, especially at larger radii. O VI broadly agrees with observations for $M_* > 10^{9.5} M_\odot$ at multiple radii while lower mass systems show $N_{\text{O VI}}$ values roughly ~ 3 dex lower. The cool regime (H I, Mg II and Si II) has high column density in the centre for all haloes but drops off significantly above $0.2R_{200c}$. $N_{\text{Mg II}}$ and $N_{\text{Si II}}$ are higher in systems with $M_* > 10^{9.5}$ than in lower mass systems at large radii. H I has larger scatter in more massive haloes but no significant dependence of the median $N_{\text{H I}}$ on stellar mass.

will be more gas at $10^5 \text{ K} - 10^{5.5} \text{ K}$ where C IV and O VI is commonly found.

We see good agreement with observations in our $10^{9.7} M_\odot$ stellar mass halo. For $M_* = 10^{10.1} M_\odot$, we find agreement with the limited data available.

There are few detections of $N_{\text{O VI}}$ at stellar masses below $\leq 10^{9.3} M_\odot$. Our dwarf simulations predict no detectable absorption associated with haloes outside the very centre of these haloes likely a combination of low metallicity because of weak outflows and low temperatures. For $M_* = 10^{9.7} M_\odot$ and $M_* = 10^{10.1} M_\odot$, our simulations underpredict $N_{\text{O VI}}$ in most observations except in the central CGM. At these stellar masses, the O VI column density decreases

with radius more steeply than observations indicate. At $10^{10.8} M_\odot$, we find the best agreement with detections from observations, but our median and scatter low above most upper limits.

For Mg II and Si II, the column densities at small radii are high, with a steep decrease between $0.2 - 0.3R_{200c}$ for $M_* \leq 10^{10.1} M_\odot$. We notice a shallower decrease in median and an increase in scatter for both of these ions for $M_* = 10^{10.8} M_\odot$, similar to $N_{\text{H I}}$.

Data for stellar masses $\leq 10^{9.7} M_\odot$ are fairly sparse, leading to a lack of detections to compare with. Above $10^{10.1} M_\odot$, we find good agreement with detections in the inner $0.25R_{200c}$ for $N_{\text{Si II}}$. At $M_* = 10^{10.8} M_\odot$, we see an overprediction at small radii for both Mg II

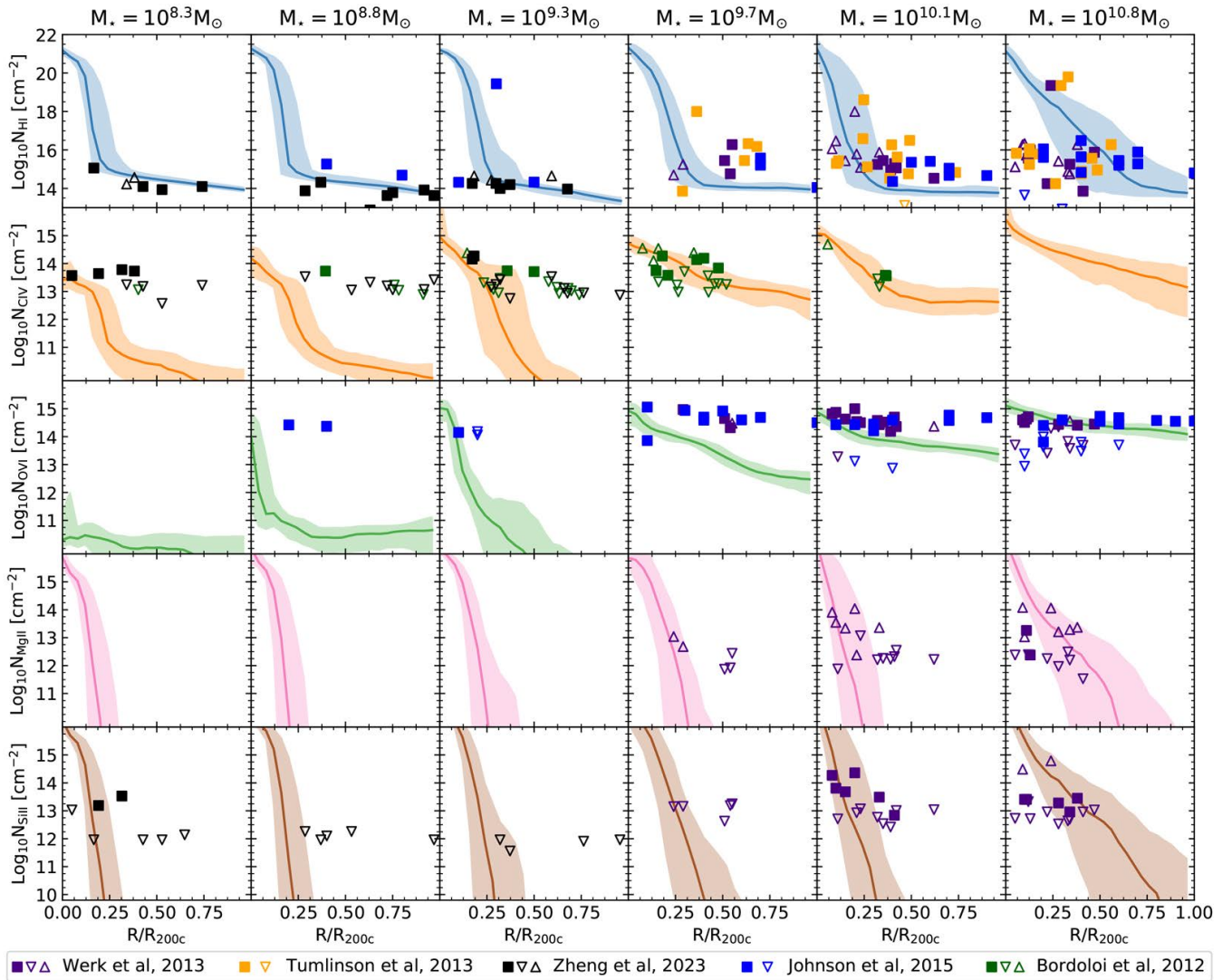


Figure 7. Radial profiles of H I and ion column densities, where the radius is normalised by R_{200c} , for the same haloes as in Fig. 5. The median is shown by solid curves and the 16th and 84th percentiles are shown as shaded regions. From top to bottom, each row shows the radial profile for $N_{\text{H I}}$, $N_{\text{C IV}}$, $N_{\text{O VI}}$, $N_{\text{Mg II}}$ and $N_{\text{Si II}}$. Our radial profiles are compared with observational data, binned within $10^{8.0} M_{\odot} < M_{\star} < 10^{11} M_{\odot}$ in equal intervals of 0.5 dex, increasing from left to right. Haloes from our simulations are selected to have stellar masses in the middle of these mass bins. Similarly to Figure 6, the ISM is removed from the simulations. The column density of all ions increases with stellar mass in the outer CGM. Our column density for H I agrees with most observational detections in haloes with $M_{\star} < 10^{9.7} M_{\odot}$. We see underpredictions at radii $R > 0.5R_{200c}$ for $10^{9.7} M_{\odot}$ and $10^{10.1} M_{\odot}$, and an overprediction at low radii at $M_{\star} = 10^{10.8} M_{\odot}$. C IV agrees with observations at small radii ($R < 0.4R_{200c}$) for $M_{\star} \geq 10^{9.3} M_{\odot}$ while O VI is slightly under-produced at all stellar masses except the most massive ($M_{\star} = 10^{10.8} M_{\odot}$). Mg II and Si II follow similar radial profiles with sharp drop off between $\sim 0.2R_{200c} - 0.3R_{200c}$. There are few observational detections below $10^{10.1} M_{\odot}$ to compare with our column densities. We do however find reasonable agreement with observations in the two most massive haloes studied.

and Si II. We find that our simulations match detections beyond a radius of $0.25R_{200c}$ for Si II.

4.3 Relation to Physical Properties

To better understand the properties of gas that give rise to these absorption line features, Figure 8 shows the physical properties as in Figure 3 weighted by the mass of C IV (yellow squares), O VI (blue upward triangles) and Mg II (orange downward arrows). This is to highlight the physical properties traced by the ions we have selected. H I- and Si II-weighted values are not shown for clarity, but resemble Mg II weighted properties. We computed the ion-weighted median values of these properties between $0.3 \leq R/R_{200c} \leq 1.0$.

This excludes the central CGM, containing primarily cool, relatively dense, metal-rich and mostly inflowing gas.

We see gas traced by O VI at higher temperatures than C IV, and gas traced by Mg II is the coolest, as we would expect for lower ionization states. We see a distinct change in temperature at $M_{200c} = 10^{11} M_{\odot}$, for O VI and C IV. Their temperature increases by ~ 0.7 dex, corresponding to their collisional ionization equilibrium values (see e.g. [Strawn et al. 2023](#)). We find that the temperature (density) of C IV and O VI lies around $\sim 10^5$ K ($\sim 10^{-4} \text{ cm}^{-3}$) and $\sim 10^{5.5}$ K ($\sim 10^{-4.8} \text{ cm}^{-3}$), respectively, for $M_{200c} > 10^{11} M_{\odot}$.

Mg II, as well as H I and Si II, are found consistently at low temperatures of $\sim 10^4$ K. The densities of the gas probed by these low ionization state ions range from $\sim 10^{-3.5} - \sim 10^{-2.5} \text{ cm}^{-3}$ indepen-

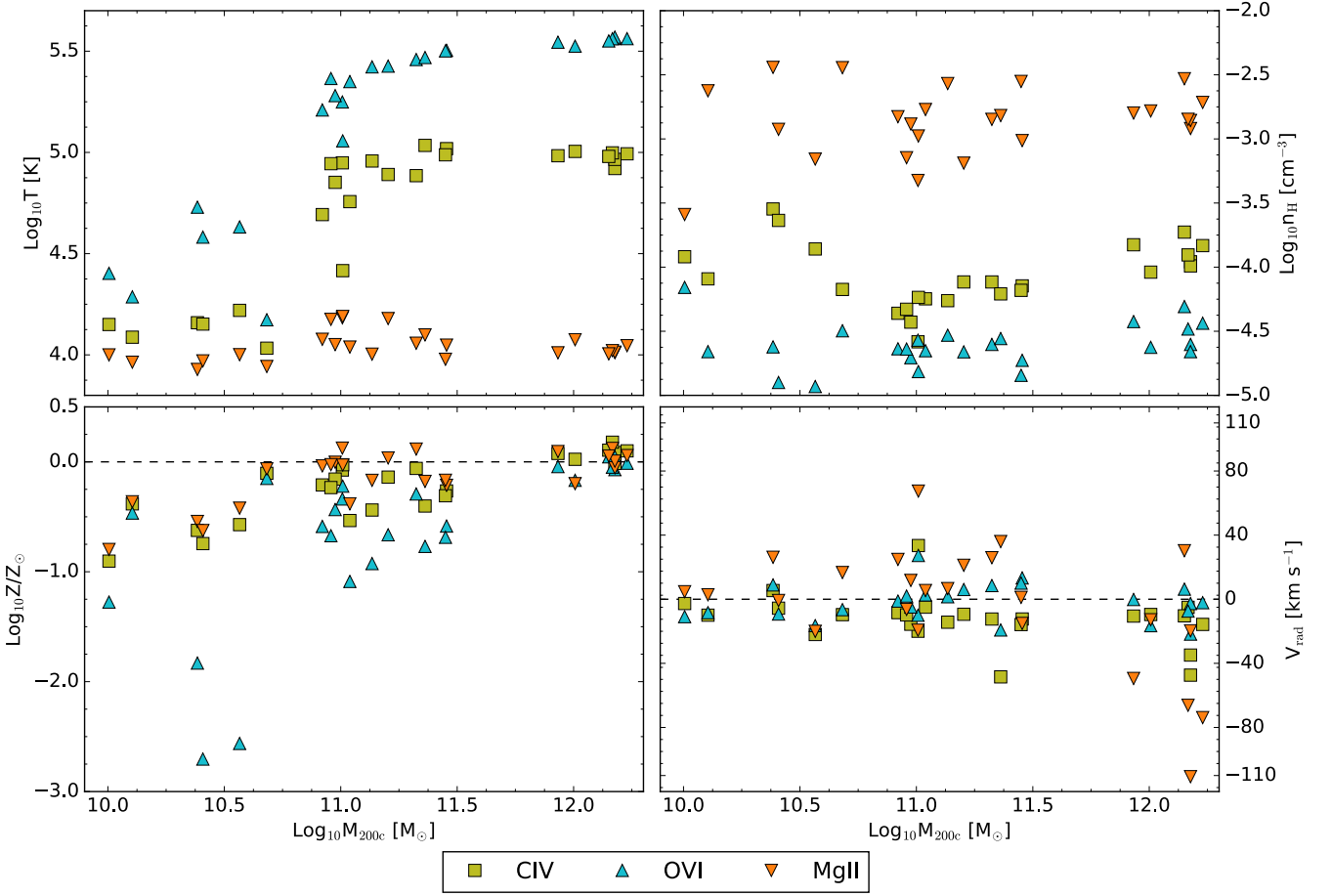


Figure 8. Temperature (top, left), hydrogen number density (top, right), metallicity (bottom, left) and radial velocity (bottom, right) against M_{200c} as in Fig. 3. We show the median values weighted by the ion mass of C IV (yellow squares), O VI (blue upward triangles) and Mg II (orange downward triangles) and measured between $0.3 \leq R/R_{200c} \leq 1.0$. H I and Si II are similar to Mg II and are omitted for clarity. We see a sharp increase in temperature of O VI and C IV at $M_{200c} = 10^{11} M_{\odot}$, indicating a transition from photo-ionization equilibrium to collisional ionization equilibrium. The metallicity is higher in more massive haloes for all ions. The density and radial velocity show no significant dependence on halo mass. There are significant differences between the temperature, the density, the metallicity and the radial velocity of these ions. Mg II remains at 10^4 K for all haloes, at relatively high densities. C IV and O VI trace higher temperatures up to 10^5 K and $10^{5.5}$ K, respectively, in more diffuse gas, which explains its ubiquity in the final three rows of Figure 5.

dent of mass. These ions populate the coolest and densest parts of the outer 70% of the CGM. Additionally, Figure 5 shows Mg II and Si II in a largely filamentary structure in the most massive halo. By comparing to the most massive halo in in Figure 2, we can see that filaments found in the halo are at cooler temperatures and higher densities than the rest of the halo, indicating Mg II and Si II trace cool and dense filamentary structure.

The metallicity of the gas traced by C IV, O VI and Mg II is higher in more massive haloes. C IV and Mg II trace higher metallicity gas than O VI at fixed halo mass. This is because O VI traces more diffuse gas which is typically more metal poor. Above $\geq 10^{12} M_{\odot}$, all ions are tracing approximately solar metallicity gas.

We find that the ion-weighted radial velocity does not show a strong dependence on halo mass. The median O VI radial velocity has no preferred direction and is divided equally between slightly inflowing and slightly outflowing gas, while the median C IV is inflowing for most of our haloes. Mg II primarily traces outflowing gas at intermediate halo masses ($10^{10.5} M_{\odot} - 10^{11.5} M_{\odot}$). Mg II has previously been found to be dominated by inflows in the inner 60 kpc of $10^{11.5} M_{\odot} - 10^{12} M_{\odot}$ haloes (DeFelippis et al. 2021). Interestingly,

we analyzed the median radial velocity of Mg II and found inflows dominating above $10^{11.5} M_{\odot}$ in the outer 70% of the CGM.

5 SUMMARY AND DISCUSSION

We have investigated the role the halo mass plays in changing the physical properties of the CGM in the Auriga suite of cosmological simulations. This included an analysis of the temperature, density, metallicity and radial velocity of the CGM for halo masses ranging from $10^{10} M_{\odot} - 10^{12} M_{\odot}$. We additionally analysed the column density of H I and the metal ions C IV, O VI, Mg II and Si II as a function of stellar mass and radius, and compared to observational data. While this is for one galaxy formation model only, it can give us an idea of what to expect in future observations and can additionally be used to constrain models.

We summarise the results of our study below:

- The CGM of dwarf galaxies ($\sim 10^{10} M_{\odot}$) features a narrow radial temperature range. The scatter, defined as the range between the 16th and 84th percentile of our data, in temperature increases from ~ 0.5 dex in $10^{10} M_{\odot}$ haloes to ~ 1.5 dex in $10^{12} M_{\odot}$ haloes.

This indicates the multiphase nature of the CGM is dependent on the halo mass.

- The median and scatter of the volume-weighted density shows no clear dependence on halo mass. The scatter of the mass-weighted density does show some increase with halo mass.

- The CGM of all of our simulated dwarf galaxies is extremely metal deficient at large radii due to weak outflows up to a halo mass of $10^{11} M_{\odot}$. The metallicity in the centre of the CGM is high but does not reach solar values. The scatter in metallicity is large in within single haloes and from halo-to-halo with metallicities ranging from less than $10^{-5} Z_{\odot}$ up to $10^{-0.5} Z_{\odot}$. Haloes with masses on the order of $\sim 10^{12} M_{\odot}$ have solar to super-solar metallicity in their centres, and have significantly more metal enriched gas than dwarfs at large radii and exhibit large scatter in metallicity. Most of the gas in Milky Way-mass haloes reaches metallicities between 10 – 100% solar, though there are some lower metallicities above $0.5R_{200c}$.

- We found low outflow velocities in our dwarf galaxies, which means that gas is not efficiently transported out of the inner CGM to larger radii. The gas inflow velocities around dwarf galaxies are much higher. The inflow and outflow velocities increase with halo mass. Above halo masses of $\sim 10^{11.5} M_{\odot}$, the inflow and outflow velocities are roughly equal out to at least the virial radius.

- The median column densities of our cool regime (H I, Mg II and Si II) are significantly higher than column densities derived from observations in the inner $0.2R_{200c}$. $N_{\text{H I}}$ decreases to between $10^{14} \text{ cm}^{-2} - 10^{15} \text{ cm}^{-2}$ at $0.6R_{200c}$, in reasonable agreement with observations. $N_{\text{Mg II}}$ and $N_{\text{Si II}}$ drop off sharply outside of $0.2R_{200c}$ at stellar masses $M_{\star} \leq 10^{10} M_{\odot}$. There are not enough observational detections to compare to for Si II below $10^{9.5} M_{\odot}$. Above $10^{9.5} M_{\odot}$, we find reasonable agreement with detections of Si II out to $0.4R_{200c}$ and upper limits at larger radii.

- The median column density of C IV agrees with observational detections for $R < 0.2R_{200c}$ in all our simulated haloes. $N_{\text{C IV}}$ decreases at larger radii for all haloes, but shows a very steep decrease in $M_{\star} < 10^{9.5} M_{\odot}$ systems, below the few available detections between $0.2R_{200c} - 0.4R_{200c}$. The median O VI column density largely matches observations at high stellar masses (above $10^{9.5} M_{\odot}$) but underpredicts them for stellar masses below $10^{9.5} M_{\odot}$. The column densities of both C IV and O VI in galaxy haloes above a stellar mass of $10^{9.5} M_{\odot}$ decrease by about 1 dex on average from the centre out to $\sim 0.6R_{200c}$ which is not seen in observations.

- We investigated the properties of gas probed by C IV, O VI and Mg II at radii greater than $0.3R_{200c}$ and found that each ion corresponds to its collisional ionization equilibrium temperature of 10^5 K , $10^{5.5} \text{ K}$ and 10^4 K respectively (e.g. Fig.2 from [Strawn et al. 2023](#)). A clear transition from photo-ionization equilibrium to collisional ionization equilibrium for C IV and O VI is seen at a halo mass of $10^{11} M_{\odot}$, featuring a temperature increase from $\sim 10^{4.1} \text{ K}$ to $\sim 10^5 \text{ K}$ for C IV and $\sim 10^{4.5} \text{ K}$ to $\sim 10^{5.5} \text{ K}$ for O VI. Mg II is found in gas that is consistently cool ($\sim 10^4 \text{ K}$) and at densities between $\sim 10^{-3.5} \text{ cm}^{-3} - \sim 10^{-2} \text{ cm}^{-3}$. The ion-weighted metallicity shows that Mg II and C IV reside in higher metallicity gas than O VI for all haloes up to $10^{12} M_{\odot}$. The ion-weighted radial velocity shows mostly outflowing Mg II and inflowing O VI gas between halo masses of $10^{10.5} M_{\odot}$ and $10^{11.5} M_{\odot}$. For halo masses greater than $10^{11.5} M_{\odot}$, all metal ions we investigated are preferentially associated with inflowing gas likely tracing large-scale fountain flows.

Our resolution tests show similar range scatter across all physical properties irrespective of the resolution of the simulation. In our higher and lower resolution simulations, we see the same trends for the physical properties as a function of halo mass: median tempera-

ture (metallicity) increases from $10^{4.5} \text{ K}$ to $\sim 10^6 \text{ K}$ ($< 10^{-5} - 10^0$) also the scatter increases (decreases) from ~ 0.2 dex to 1.5 dex (~ 4 dex to 0.3 dex). The density shows no significant dependence on halo mass nor the median radial velocity. The radial velocity scatter increases from $< 10 \text{ km/s}$ to $\sim 70 \text{ km/s}$ with halo mass. Additionally, trends in column density – increasing with halo mass, decreasing radial profiles and underpredictions compared to observations – are still present in the level 4 and level 2 simulations. The median and scatter of the column density of all our ions does not deviate much from the level 3 simulations.

A similar study by [Hani et al. \(2019\)](#) studied the haloes of 40 L^* galaxies in Auriga with stellar mass between $10^{10.3} M_{\odot} - 10^{11.1} M_{\odot}$. They found that the gas and metal content of the CGM show a tight correlation with the stellar mass of the host galaxy, similar to our findings. Contrarily, they found the ionization of metals in the CGM is independent of stellar mass, with covering fractions of H I, Si II, C IV and O VI showing no clear dependence on stellar mass. This seems contradictory to what we find. Haloes of increasing stellar mass feature higher column densities for those ions. However, this may be explained by the smaller stellar mass range ($2.1 \leq M_{\star} [10^{10} M_{\odot}] \leq 11.7$) and halo mass range ($0.5 \leq M_{\star} [10^{12} M_{\odot}] \leq 2.0$) of [Hani et al. \(2019\)](#). Our results show that for a much larger range of stellar masses the column density changes in both median and scatter specifically for high ionization states such as C IV and O VI.

In a different suite of simulations, called NIHAO ([Wang et al. 2015](#)), [Gutcke et al. \(2017\)](#) used a halo mass range similar to our own of $10^{9.7} M_{\odot} - 10^{12.5} M_{\odot}$ and analysed the column density of H I and O VI. Using the same self-shielding approximation as our simulations ([Rahmati et al. 2013](#)), they found better agreement between their H I column densities and observations than for O VI. Additionally, [Gutcke et al. \(2017\)](#) show that the trend of O VI with luminosity (a proxy for stellar mass) in their simulations agrees with observations but their radial dependence of O VI underpredicts the observations. In comparison to our work, the column density of H I follows a similar trend as a function of impact parameter reaching a plateau of $\sim 10^{14} \text{ cm}^{-2}$. We find lower O VI column densities than [Gutcke et al. \(2017\)](#) out to the virial radius in haloes with $M_{200c} < 10^{11} M_{\odot}$. At higher halo masses, [Gutcke et al. \(2017\)](#) find the radial dependence of O VI has a narrow range of values between $10^{13} \text{ cm}^{-2} - 10^{14} \text{ cm}^{-2}$. We find column densities higher than this, extending to the virial radius.

[Hummels et al. \(2013\)](#) conducted similar work investigating the column density of H I, Si II, C IV and O VI in the CGM of a Milky Way-mass galaxy with different stellar feedback prescriptions. They find that even minimal feedback can still push metals out to large radii ($> 50 \text{ kpc}$) but there is a lack of multiphase gas which underproduces observed ions - this is notably true of O VI which did not match any of their models. This is different to our results, which show column densities of O VI in Milky Way mass haloes that better match observations at large radii. They additionally found that increasing thermal feedback from the galaxy to very high values increased the O VI column density but still underpredicted observations.

Similar underpredictions for O VI and H I were found in the FIRE-2 suite of MHD simulations from [Ji et al. \(2020\)](#) who found that adding cosmic ray feedback in Milky Way mass haloes increased columns in line with observational detections and limits.

In order to compute the column density in our simulations, we calculated the metal ion mass fraction in post-processing based on tables generated by [Hummels et al. \(2017\)](#) using CLOUDY ([Ferland et al. 2017](#)). Producing mock spectra for these simulations utilising post-processing tools such as TRIDENT ([Hummels et al. 2017](#)) would allow us to bring our simulation analysis closer to observational data

instead of comparing to derived quantities. Hafen et al. (2024) used TRIDENT to compare synthetic absorption spectra from three different simulation sets. They found reasonable agreement between the density, temperature and metallicity derived from synthetic absorption spectra of uniform clouds and multi-cloud systems, and the source properties used to generate synthetic absorption spectra to within 0.1 dex. Mock spectra would provide us with a more robust method of comparison between observations and simulations and increase the amount of observational data we can use.

Furthermore, previous studies have shown that background or foreground absorbers may be incorrectly attributed to a halo if their line-of-sight velocity falls within the observational velocity range, usually $\pm 500 \text{ km s}^{-1}$, whilst the gas originates from different haloes outside of the virial radius (Ho et al. 2020; Weng et al. 2024). Our column densities were measured along a restricted line-of-sight depth of $2R_{200c}$. This could potentially account for discrepancies between our column densities and the observations we compared with, as Weng et al. (2024) finds that larger radii from the centre increases the line-of-sight contribution from satellites, other haloes and the IGM.

Our results likely depend on specific modelling choices in the Auriga galaxy formation model. Varying certain aspects of our simulations in the future will help to better determine how sensitive our results are to these changes. Potentially relevant subgrid model variations include a kinetic AGN feedback model, cosmic ray feedback, an improved ISM model that incorporates multi-phase gas physics, and a stellar feedback model that is more efficient in dwarf galaxies. Comparisons between CGM predictions and observables are a promising way forward to constrain and distinguish between different galaxy formation models. Additional physical processes such as incorporating cosmic ray feedback in simulations has shown that outflow rates in dwarf galaxies increase and agree more with observations (Dashyan & Dubois 2020; Farcy et al. 2022; DeFelippis et al. 2024).

ACKNOWLEDGEMENTS

FvdV is supported by a Royal Society University Research Fellowship (URF\R1\191703). RG acknowledges financial support from an STFC Ernest Rutherford Fellowship (ST/W003643/1). Software used for this work includes numpy (Harris et al. 2020), matplotlib (Hunter 2007). The simulations were performed on computing resources provided by the Max Planck Computing and Data Facility in Garching.

DATA AVAILABILITY

The Auriga suite of cosmological simulations, including all simulations used in this work, are available at the following website <https://wwwmpa.mpa-garching.mpg.de/auriga/dataspecs.html>. The absorption line tables used in this study were part of the TRIDENT project and are available at the following website https://trident-project.org/data/ion_table/.

REFERENCES

Agertz O., et al., 2020, *MNRAS*, 491, 1656
 Anand A., Nelson D., Kauffmann G., 2021, *MNRAS*, 504, 65
 Appleby S., Davé R., Sorini D., Storey-Fisher K., Smith B., 2021, *MNRAS*, 507, 2383

Behroozi P. S., Wechsler R. H., Conroy C., 2013, *ApJ*, 770, 57
 Bordoloi R., et al., 2014, *ApJ*, 796, 136
 Burchett J. N., et al., 2016, *ApJ*, 832, 124
 Dashyan G., Dubois Y., 2020, *A&A*, 638, A123
 Davis M., Efstathiou G., Frenk C. S., White S. D. M., 1985, *ApJ*, 292, 371
 DeFelippis D., Bouché N. F., Genel S., Bryan G. L., Nelson D., Marinacci F., Hernquist L., 2021, *ApJ*, 923, 56
 DeFelippis D., Bournaud F., Bouché N., Tollet E., Farcy M., Rey M., Rosdahl J., Blaizot J., 2024, *MNRAS*, 530, 52
 Farcy M., Rosdahl J., Dubois Y., Blaizot J., Martin-Alvarez S., 2022, *MNRAS*, 513, 5000
 Faucher-Giguère C.-A., Lidz A., Zaldarriaga M., Hernquist L., 2009, *ApJ*, 703, 1416
 Ferland G. J., et al., 2017, *Rev. Mex. Astron. Astrofis.*, 53, 385
 Fox A. J., Wakker B. P., Savage B. D., Tripp T. M., Sembach K. R., Bland-Hawthorn J., 2005, *ApJ*, 630, 332
 Frenk C. S., White S. D. M., Davis M., Efstathiou G., 1988, *ApJ*, 327, 507
 Girelli G., Pozzetti L., Bolzonella M., Giocoli C., Marulli F., Baldi M., 2020, *A&A*, 634, A135
 Gnat O., Sternberg A., 2007, *ApJS*, 168, 213
 Grand R. J. J., et al., 2017, *MNRAS*, 467, 179
 Grand R. J. J., Fragkoudi F., Gómez F. A., Jenkins A., Marinacci F., Pakmor R., Springel V., 2024, *arXiv e-prints*, p. arXiv:2401.08750
 Gutcke T. A., Stinson G. S., Macciò A. V., Wang L., Dutton A. A., 2017, *MNRAS*, 464, 2796
 Gutcke T. A., Pakmor R., Naab T., Springel V., 2021, *MNRAS*, 501, 5597
 Hafen Z., et al., 2020, *MNRAS*, 494, 3581
 Hafen Z., et al., 2024, *MNRAS*, 528, 39
 Hani M. H., Ellison S. L., Sparre M., Grand R. J. J., Pakmor R., Gomez F. A., Springel V., 2019, *MNRAS*, 488, 135
 Harris C., Millman K., van der Walt S. e. a., 2020, *Nature*, 582, 357
 Ho S. H., Martin C. L., Schaye J., 2020, *ApJ*, 904, 76
 Hummels C. B., Bryan G. L., Smith B. D., Turk M. J., 2013, *MNRAS*, 430, 1548
 Hummels C. B., Smith B. D., Silvia D. W., 2017, *ApJ*, 847, 59
 Hunter J. D., 2007, *Computing in Science & Engineering*, 9, 90
 Ji S., et al., 2020, *MNRAS*, 496, 4221
 Johnson S. D., Chen H.-W., Mulchaey J. S., 2015, *MNRAS*, 449, 3263
 Johnson S. D., Chen H.-W., Mulchaey J. S., Schaye J., Straka L. A., 2017, *ApJ*, 850, L10
 Kannan R., Vogelsberger M., Marinacci F., McKinnon R., Pakmor R., Springel V., 2019, *MNRAS*, 485, 117
 Katz H., 2022, *MNRAS*, 512, 348
 Kereš D., Katz N., Weinberg D. H., Davé R., 2005, *MNRAS*, 363, 2
 Lehner N., et al., 2013, *ApJ*, 770, 138
 Machado R. E. G., Tissera P. B., Lima Neto G. B., Sodré L., 2018, *A&A*, 609, A66
 Mathur S., Gupta A., Das S., Krongold Y., Nicastro F., 2021, *ApJ*, 908, 69
 Mo H., van den Bosch F. C., White S., 2010, *Galaxy Formation and Evolution*. Cambridge University Press
 Moster B. P., Somerville R. S., Maulbetsch C., van den Bosch F. C., Macciò A. V., Naab T., Oser L., 2010, *ApJ*, 710, 903
 Muratov A. L., Kereš D., Faucher-Giguère C.-A., Hopkins P. F., Quataert E., Murray N., 2015, *MNRAS*, 454, 2691
 Oppenheimer B. D., Davé R., Kereš D., Fardal M., Katz N., Kollmeier J. A., Weinberg D. H., 2010, *MNRAS*, 406, 2325
 Pakmor R., Springel V., Bauer A., Mocz P., Munoz D. J., Ohlmann S. T., Schaal K., Zhu C., 2016, *MNRAS*, 455, 1134
 Peebles M. S., Werk J. K., Tumlinson J., Oppenheimer B. D., Prochaska J. X., Katz N., Weinberg D. H., 2014, *ApJ*, 786, 54
 Peebles M., et al., 2019, *BAAS*, 51, 368
 Planck Collaboration et al., 2014, *A&A*, 571, A16
 Portinari L., Chiosi C., Bressan A., 1998, *A&A*, 334, 505
 Rahmati A., Pawlik A. H., Raičević M., Schaye J., 2013, *MNRAS*, 430, 2427
 Ranjan A., et al., 2022, *A&A*, 661, A134
 Sales L. V., Wetzel A., Fattahi A., 2022, *Nature Astronomy*, 6, 897
 Sanchez N. N., Werk J. K., Tremmel M., Pontzen A., Christensen C., Quinn T., Cruz A., 2019, *ApJ*, 882, 8

- Schaye J., et al., 2015, *MNRAS*, **446**, 521
Springel V., 2010, *MNRAS*, **401**, 791
Springel V., Hernquist L., 2003, *MNRAS*, **339**, 289
Strawn C., Roca-Fàbrega S., Primack J., 2023, *MNRAS*, **519**, 1
Tchernyshyov K., et al., 2022, *ApJ*, **927**, 147
Tumlinson J., et al., 2011, *Science*, **334**, 948
Tumlinson J., et al., 2013, *ApJ*, **777**, 59
Tumlinson J., Peebles M. S., Werk J. K., 2017, *ARA&A*, **55**, 389
Vogelsberger M., Genel S., Sijacki D., Torrey P., Springel V., Hernquist L., 2013, *MNRAS*, **436**, 3031
Wang P., Abel T., 2008, *ApJ*, **672**, 752
Wang L., Dutton A. A., Stinson G. S., Macciò A. V., Penzo C., Kang X., Keller B. W., Wadsley J., 2015, *MNRAS*, **454**, 83
Weng S., Péroux C., Ramesh R., Nelson D., Sadler E. M., Zwaan M., Bollo V., Casavecchia B., 2024, *MNRAS*, **527**, 3494
Werk J. K., Prochaska J. X., Thom C., Tumlinson J., Tripp T. M., O’Meara J. M., Peebles M. S., 2013, *ApJS*, **204**, 17
Werk J. K., et al., 2016, *ApJ*, **833**, 54
Wiersma R. P. C., Schaye J., Smith B. D., 2009, *MNRAS*, **393**, 99
Wright R. J., Lagos C. d. P., Power C., Correa C. A., 2021, *MNRAS*, **504**, 5702
Zheng Y., Emerick A., Putman M. E., Werk J. K., Kirby E. N., Peek J., 2020, *ApJ*, **905**, 133
Zheng Y., et al., 2024, *ApJ*, **960**, 55
van de Voort F., Schaye J., 2012, *MNRAS*, **423**, 2991

APPENDIX A: HALO AND GALAXY PROPERTIES

In Table A1, we outline global properties from the most massive halo in each of our simulations, selected to be relatively isolated. These data outline the halo name, virial mass, virial temperature, virial radius, star formation rate and stellar mass of the most-massive halo within the zoom-in region of each simulation.

This paper has been typeset from a \LaTeX file prepared by the author.

Halo ID ^a	Log ₁₀ M _{200c} ^b [M _⊙]	T _{vir} ^c [K]	R _{200c} ^d (kpc)	SFR ^e [M _⊙ /yr]	Log ₁₀ M _★ ^f [M _⊙]
<i>M</i> _{200c} = 10 ¹⁰ M _⊙ – 10 ¹¹ M _⊙ Haloes					
halo_0	10.00	4.35	45.58	0.00	7.46
halo_2	10.68	4.84	76.67	0.46	9.36
halo_6	10.38	4.61	61.00	0.10	8.48
halo_8	10.10	4.46	49.22	0.05	8.48
halo_9	10.56	4.78	70.10	0.16	8.85
halo_11	10.40	4.65	62.11	0.08	8.34
<i>M</i> _{200c} = ~10 ¹¹ M _⊙ – 10 ¹² M _⊙ Haloes					
halo_0	11.00	4.89	98.36	0.79	9.77
halo_1	11.32	5.14	125.47	2.06	10.08
halo_2	11.13	5.11	108.48	0.78	9.74
halo_3	11.36	5.21	129.18	1.15	10.08
halo_4	11.45	5.33	138.67	1.43	10.08
halo_5	11.45	5.35	138.17	0.60	10.14
halo_6	10.97	4.94	96.06	0.52	9.72
halo_7	11.20	5.07	114.38	1.41	9.92
halo_8	11.03	5.06	100.82	0.46	9.53
halo_9	11.00	4.89	98.47	0.62	9.63
halo_10	10.92	4.88	92.07	0.47	9.55
halo_11	10.95	4.98	94.72	0.89	9.67
<i>M</i> _{200c} ≥ 10 ¹² M _⊙ Haloes					
halo_L8	11.93	5.57	200.20	5.71	10.82
halo_6	12.00	5.58	211.83	2.71	10.81
halo_16	12.18	5.81	241.53	4.20	10.96
halo_21	12.15	5.71	236.69	10.27	10.96
halo_23	12.17	5.71	241.50	4.60	10.97
halo_24	12.17	5.76	239.57	7.67	10.95
halo_27	12.23	5.70	251.40	4.20	11.01

Table A1. Properties of our most massive haloes in each of our simulations. a) simulation reference name b) halo mass c) virial temperature d) virial radius of halo e) stellar mass f) star formation rate.